Zinc-Ion Batteries

International Edition: DOI: 10.1002/anie.201912203
German Edition: DOI: 10.1002/ange.201912203

A Deep-Cycle Aqueous Zinc-Ion Battery Containing an Oxygen-Deficient Vanadium Oxide Cathode

Meng Liao, Jiawei Wang, Lei Ye, Hao Sun, Yunzhou Wen, Chuang Wang, Xuemei Sun, Bingjie Wang, and Huisheng Peng**

Abstract: *Rechargeable aqueous zinc-ion batteries are attractive because of their inherent safety, low cost, and high energy density. However, viable cathode materials (such as vanadium oxides) suffer from strong Coulombic ion–lattice interactions with divalent* Zn^{2+}*, thereby limiting stability when cycled at a high charge/discharge depth with high capacity. A synthetic strategy is reported for an oxygen-deficient vanadium oxide cathode in which facilitated* Zn^{2+} *reaction kinetic enhance capacity and* Zn^{2+} *pathways for high reversibility. The benefits for the robust cathode are evident in its performance metrics; the aqueous Zn battery shows an unprecedented stability over 200 cycles with a high specific capacity of approximately 400 mAh* g^{-1}*, achieving 95% utilization of its theoretical capacity, and a long cycle life up to 2000 cycles at a high cathode utilization efficiency of 67%. This work opens up a new avenue for synthesis of novel cathode materials with an oxygen-deficient structure for use in advanced batteries.*

Achieving low-cost and safe batteries with high energy density is promising for large-scale energy storage applications.[1] Within this research area, aqueous Li- and Na-ion batteries in mild aqueous electrolytes are primarily explored because of their intrinsic safety and environmentally friendly features.[2] Unfortunately, electrodes for aqueous Li- and Na-ion batteries generally exhibit low capacities (<150 mAh g^{-1}), and their applications are thus limited. To this end, Zn^{2+} storage chemistry in mild aqueous electrolytes has recently attracted interest because metallic zinc anodes exhibit a low redox potential of −0.76 V (versus standard hydrogen electrode), a high theoretical capacity of 820 mAh g^{-1}, and desirable Zn/Zn^{2+} reversibility in mild aqueous electrolytes.[3,4] The development of aqueous zinc-ion batteries (AZIBs), however, still faces key challenges related to the design of suitable cathode materials that match high-capacity Zn anodes. To date, manganese oxides,[5–11] vanadium-based compounds,[12–20] Prussian blue analogues,[21] quinone analogues,[22] and polyanion compounds[23] have been studied as viable cathodes for AZIBs. Among them, vanadium oxides are mostly explored because of their high theoretical capacities (generally >300 mAh g^{-1}), stable layered structure, and low cost.[24,25]

Despite the aforementioned promising properties, such materials typically suffer from strong electrostatic interactions with divalent Zn^{2+}, which can cause sluggish reaction kinetics and inhibit reversible Zn^{2+} storage.[4,26] In particular, the electronegative oxygen atoms in host lattice (for example, vanadium oxide) tend to trap a certain amount of Zn^{2+} during cycling, which may disable the subsequent Zn^{2+} release (charging) process, and eventually aggravate capacity fading with poor rate performance. Consequently, with the insertion of a large amount of Zn^{2+} (that is, when cycled with a high charge/discharge depth) the vanadium-oxide-based cathodes in AZIBs generally exhibit low stability. Although there are several reports about high cycling performances of >1000 cycles in vanadium-oxide-based cathodes, such stabilities are only achieved at low utilization ($<50\%$) of the theoretical cathode capacity with limited capacity (generally <250 mAh g^{-1}).[4,24] To the best of our knowledge, the stable cycling of a vanadium oxide cathode with high utilization of $>90\%$ has never been realized. A breakthrough is urgently needed to achieve high cathodic capacity of AZIB cathodes in mild electrolytes.

Herein, we tackle these limitations by exploring oxygen-deficient vanadium oxide cathodes that favor divalent Zn^{2+} reaction kinetics to achieve high capacities as well as improved Zn^{2+} pathways for facile Zn^{2+} storage/release with high reversibility (Figure 1a). The synthesized oxygen-deficient V_6O_{13} (O_d-VO), with alternating single and double vanadium oxide layers, was enriched with oxygen vacancies to create more divalent cation-intercalating sites and thereby enhance capacity. The partial extraction of electronegative oxygen from the V_6O_{13} lattice was effective for boosting the reversibility of Zn^{2+} storage chemistry through electrochemical performances and simulations. The resulting aqueous Zn battery displayed high capacities (280–400 mAh g^{-1}) and long-term cyclability (up to 2000 cycles) at $>99\%$ Coulombic efficiency (CE). Impressively, O_d-VO afforded high stability (≥ 200 cycles) even with a high utilization of about 95% (ca. 400 mAh g^{-1}, Figure 1b), which outperformed previously reported cathode materials for AZIBs. Benefiting from the binder-free nature of the O_d-VO cathode, a flexible Zn/O_d-VO battery was achieved with impressive electrochemical behavior upon mechanical deformation.

O_d-VO was synthesized through a facile solution-redox-based self-assembly method at room temperature, followed by thermal treatment in a reducing N_2/H_2 atmosphere (Supporting Information, Figure S1). O_d-VO possesses

---

[*] M. Liao, J. Wang, L. Ye, Dr. H. Sun, Y. Wen, C. Wang, Dr. X. Sun, Dr. B. Wang, Prof. H. Peng
Laboratory of Advanced Materials, State Key Laboratory of Molecular Engineering of Polymers and Department of Macromolecular Science, Fudan University
Shanghai 200438 (China)
E-mail: wangbingjie@fudan.edu.cn
penghs@fudan.edu.cn

Supporting information and the ORCID identification number(s) for the author(s) of this article can be found under: https://doi.org/10.1002/anie.201912203.

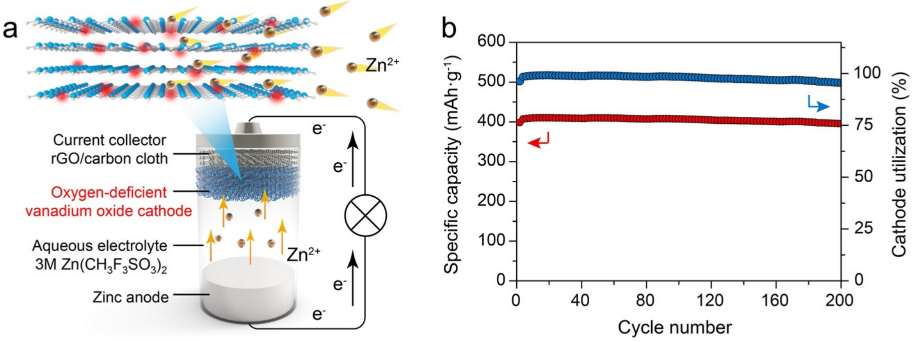

Figure 1. a) Configuration of the Zn/O_d-VO battery and its behavior during discharge; the oxygen-deficient sites (represented by red spheres) are incorporated into the vanadium oxide framework. b) Cycling performance in terms of specific capacity (red) and the corresponding cathode utilization (blue) at a current density of 200 mA g^{-1}.

a porous 3D foam morphology, as revealed by low-magnification scanning electron microscopy (SEM; Figure 2a). Energy-dispersive X-ray spectroscopy (EDS) elemental mappings of O_d-VO revealed a homogeneous distribution of V, O, and C elements across the electrode without discernible impurities (Figure S2). A highly interconnected, nano-textile-like architecture, was created by assembly of O_d-VO nanobelts on reduced graphene oxide (rGO, Figures 2b; Figure S3); rGO functioned as a porous current collector for the loaded active materials and enabled accelerated transport of electrons and ions. This internal cross-linked structure inhibited self-aggregation and permitted construction of freestanding electrodes with high stability.[27–29] The selected area electron diffraction (SAED) pattern of O_d-VO presented two diffraction rings, which correspond to the (1 1 0) and (1 2 4) planes of V_6O_{13} (Figure 2c). The SAED patterns obtained from O_d-VO revealed amorphous-like reflection rings, which were different from the contrast reflection rings of pristine V_6O_{13} (*p*-VO; Figure S4). It is suggested that O_d-VO is more disordered than *p*-VO because of the oxygen-deficient structure.

X-ray photoelectron spectroscopy (XPS) was further performed to highlight the oxygen-deficient structure of O_d-VO. The O 1s XPS spectra were deconvoluted into lattice oxygen (V−O) at 529.8 eV and hydroxy groups (V−OH) of defective oxygen at 532.1 eV (Figure 2d).[30] The increased intensity in defective oxygen of O_d-VO (ca. 37% based on the fitting areas in O 1s XPS spectra) indicated the introduction of oxygen vacancies. The normalized V 2p3 spectra of both samples demonstrated two characteristic peaks corresponding to V $2p_{1/2}$ and V $2p_{3/2}$ (Figure 2e).[31] Through subtracting the V 2p3 spectrum of O_d-VO from that of *p*-VO (bottom region, Figure 2e), two extra peaks situated at 523.1 and 515.8 eV were demonstrated to correspond to V $2p_{1/2}$ and V $2p_{3/2}$ peaks of V^{4+}, respectively, indicating the reduction of vanadium cations in O_d-VO. The oxygen-deficient structure was then evidenced by X-ray absorption near-edge spectroscopy (XANES). O K-edge XANES exhibited a weakened oscillation of post edges from O_d-VO compared with *p*-VO, as a consequence of the more disordered lattice with oxygen-deficient sites (Figure S5).[32] Moreover, the negative shift in the V $L_{2,3}$-edge XANES (Figure 2f) and Raman spectra (Figure S6) also revealed a decrease in the V valence in O_d-VO. Notably, the initial monoclinic lattice of O_d-VO remains in spite of the synthesis of the oxygen deficient structure, as demonstrated by X-ray diffraction (XRD) results (Figure S7).

To probe the role of the oxygen-deficient structure in Zn^{2+} storage/release processes, the electrochemical performance was tested in a coin cell (CR 2032) composed of an O_d-VO composite cathode, Zn foil anode, and a glass fiber separator infiltrated with 3 M $Zn(CH_3F_3SO_3)_2$ aqueous electrolyte. The cyclic voltammograms (CV) of O_d-VO between 0.2 and 1.5 V (versus Zn/Zn^{2+}) at 0.2 mV s^{-1} exhibited two pairs of redox peaks located at 1.16/0.91 V and 0.64/0.57 V (Figure S8). The overlapped CV curves of the first three cycles indicated a highly reversible Zn^{2+} (de)intercalation reaction at its initial stage. The galvanostatic charge/discharge profile of the O_d-VO is shown in Figure 3a, in which the current density and specific capacity were based on a mass loading of approximately 2 mg cm^{-2} of O_d-VO in the cathode. A high initial capacity of 410 mAh g^{-1} was achieved at a current density of 200 mA g^{-1}, which is close to that obtained at a low current density of 50 mA g^{-1} (Fig-

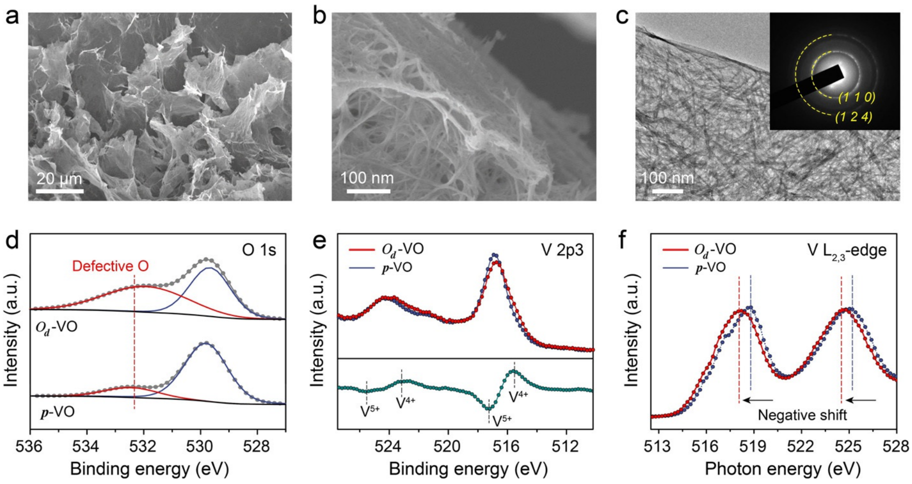

Figure 2. a) A panoramic SEM image of the O_d-VO cathode depicting a porous structure. b) An SEM image showing the nanotextile-like morphology of O_d-VO. c) A bright-field transmission electron microscopy (TEM) image (inset, SAED pattern) of O_d-VO. d) O 1s high-resolution XPS spectra. e) V 2p3 high-resolution XPS spectra. f) V $L_{2,3}$-edge XANES spectra.

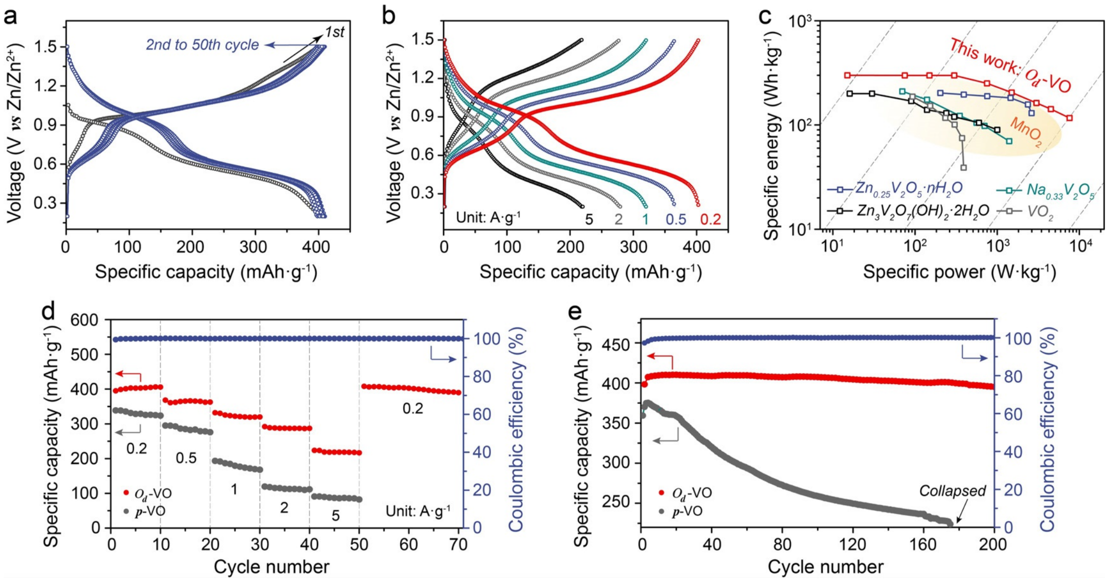

Figure 3. a) Galvanostatic discharge and charge profiles of the freestanding O_d-VO cathode at a current density of 200 mA g^{-1}. b) Galvanostatic discharge profiles of O_d-VO at increasing current densities from 200 to 5000 mA g^{-1}. c) Comparison of the Ragone plot of the Zn/O_d-VO battery with other state-of-the-art AZIBs.[5,14,17–19] Calculation of energy/power densities are based on the mass of active material in the cathode. d) Rate capability of O_d-VO and p-VO with increasing current densities and the corresponding CEs. e) Comparison of the cycling performance of O_d-VO and p-VO at 200 mA g^{-1} and the corresponding CE.

ure S9). During the initial cycle, the observed two pairs of charge/discharge plateaus corresponded to the solid–solution reaction processes associated with Zn^{2+} (de)intercalation.[4,11] In subsequent cycles, the voltage profile exhibited a reduced polarization, suggesting the activation process of O_d-VO. Notably, the Zn^{2+} (de)intercalation reactions in Zn/O_d-VO cells demonstrated high reversibility, as revealed from the reproducible voltage profiles with an average voltage of approximately 0.8 V (versus Zn/Zn^{2+}). The rate capability of O_d-VO was then investigated at increasing current densities from 0.2 to 5.0 A g^{-1} (Figure 3b). Reversible specific capacities of 401, 366, 321, and 279 mAh g^{-1} were achieved at 0.2, 0.5, 1.0, and 2.0 A g^{-1}, respectively. Even at a high rate of 5 A g^{-1}, a significantly high discharge capacity of 223 mAh g^{-1} was delivered, demonstrating an AZIB system with desirable energy density and a high power capability. Moreover, the charge/discharge profiles at various rates delivered similar shapes with small polarization, indicating high charge-transfer kinetics.

The tradeoff between energy and power densities of the O_d-VO/Zn and p-VO/Zn batteries is revealed in their Ragone plots, alongside other cathode materials for AZIBs (Figure 3c). O_d-VO exhibited a high specific energy of approximately 298 Wh kg^{-1}, based on the mass of active material in the cathode, surpassing the activity of p-VO cathodes (Figure S10). The Zn/O_d-VO cell also outperformed previously reported AZIBs over a wide range of power densities, including vanadium-based and MnO_2 cathodes. The practical realization of the rate performance was further elucidated from the rate data (Figure 3d). Upon continuous cycling with increasing current densities, the capacities of Zn/O_d-VO cells dropped only marginally at high rates and immediately recovered with their reversal. In contrast, the Zn/p-VO cell displayed an inferior capacity at each rate. The cycling stability of the O_d-VO composite was then evaluated at representative current densities of 200, 500, and 2000 mA g^{-1}. The O_d-VO composite delivered a high capacity of 398 mAh g^{-1} over 200 cycles with a CE around 100% (Figure 3e), achieving roughly 95% utilization of the theoretical capacity of V_6O_{13} (413 mAh g^{-1}; Supporting Information). To the best of our knowledge, these findings demonstrate the highest utilization in vanadium-based cathode materials for AZIBs that can be operated for ≥ 200 cycles (Supporting Information, Table S2). Upon testing at higher current densities of 500 and 2000 mA g^{-1}, the O_d-VO cathode also showed impressive capacity retention (that is, 90% after 500 cycles and 86% after 2000 cycles; Figures S11 and S12). The porous structure of O_d-VO was retained after cycling, indicating structural stability (Figure S13). Note that the rGO/carbon cloth (CC) substrates in the cathode were used as current collectors and their capacity contribution (< 1.5 mAh g^{-1}; Figure S14) was negligible compared with that of O_d-VO.

To date, cathode materials in AZIBs (such as vanadium oxides and manganese dioxides) offer a limited cycle life (≤ 200 cycles) with high cathode utilization ($\geq 90\%$) because of strong Coulombic ion–lattice interactions between divalent Zn^{2+} and host materials. With the insertion of a large amount of Zn^{2+}, chemical bonds can form between Zn and O, thereby preventing Zn^{2+} release upon charging.[4,8] These trapped Zn^{2+} ions gradually accumulate with each cycle, creating physical barriers on the cathode surface and eventually reducing the number of active sites for Zn^{2+} storage; in this way the cycling stability deteriorates. In the case of O_d-VO reported herein, electronegative oxygen atoms that interact strongly with divalent Zn^{2+} are partially extracted from the

V_6O_{13} lattice, thereby facilitating Zn^{2+} release/storage and high reversibility upon deep cycling (Figures 4 a,b). Our simulated results demonstrate that the oxygen-deficient O_d-VO structure has a thermoneutral Gibbs free energy of Zn^{2+} desorption (Table S1, Figure S15). This suggests an effortless Zn^{2+} release by the cathode, thus rendering the electrochemical active surface area, in its discharged state, fully accessible for the next charging process. In comparison, the relatively defect-free structure (*p*-VO) demonstrated a much higher Gibbs free energy of desorption, pointing to a rather difficult Zn^{2+} release, and thus leading to a deterioration in cycling stability. Electron dissipation from Zn^{2+} provides further proof for the weakened Zn–O interaction on O_d-VO compared to *p*-VO (Figure S16).

Consistent with the simulated results, the peak current density of the O_d-VO cathode was much higher than that of *p*-VO after 100 charge/discharge cycles (0.2 A g^{-1}, Figure 4 c), indicating that the former retained higher electrochemical reactivity upon cycling. Moreover, O_d-VO demonstrated smaller overpotential gaps (taking Peak 1 and 4 as indicators, Figure 4 c) than *p*-VO at each scan rate (Figure 4 d). The consistent high activity, together with the reduced polarization in O_d-VO, indicate that the introduction of oxygen vacancies facilitates a reversible Zn^{2+} storage/release mechanism. The electrochemical kinetics of O_d-VO were then analyzed by CV (Figure S17). The current (i) of the CV scan is dependent on the sweep rate (v): $i = av^b$, where a and b are variable values.[12,16] In this regard, the b values of the two pairs of redox peaks (labeled peaks 1–4) were calculated to be 0.753, 0.735, 0.677, and 0.680, respectively (Figure 4 e). This implies that the redox reactions occurring in O_d-VO are primarily limited by the chemical reaction rate rather than the ion diffusion rate.[24] The electrochemical performance of O_d-VO was further deconvoluted into an ionic diffusion contribution and surface capacitive contribution (Figure S18). As a result, 48.2 % of the total capacity was determined to be the capacitive contribution at 0.1 mV s^{-1}, which gradually increased to 77.6 % at 1.0 mV s^{-1} (Figure 4 f), suggesting rapid and highly reversible reaction kinetics, as well as high surface reactivity, on O_d-VO.

To systematically probe the enhanced Zn^{2+} storage performance, the diffusion coefficient of Zn^{2+} (D_{Zn}) in O_d-VO was determined by galvanostatic intermittent titration technique (GITT, Figures 5 a,b; Figure S19). Despite the double valence of Zn^{2+}, the average D_{Zn} values of O_d-VO at the discharge and charge plateaus were approximately 1.1×10^{-11} and 0.4×10^{-11} cm^2 S^{-1}, respectively; these values are comparable with Li diffusivity (generally at a magnitude of ca. 10^{-10} cm^2 S^{-1}). In contrast, the *p*-VO electrode exhibited an obviously lower D_{Zn} and a larger overpotential, indicating sluggish mobility during Zn^{2+} storage/release. As depicted from the charge/discharge curves (Figures 5 a; Figure S20a), the O_d-VO electrode exhibited two prolonged discharge plateaus with an enhanced capacity of approximately 160 mAh g^{-1} over *p*-VO. Considering the relatively low electronic conductivity of pristine vanadium oxides (usually with a magnitude of 10^{-5} S cm^{-1}), the efficient capacity upgrade and extent of material utilization in O_d-VO was ascribed to the highly conducting oxygen-deficient structure. It is known that the introduction of oxygen vacancies improves the diffusion of reactants while also affording extra electrons for improved capacity.[8,33] Correspondingly, a 3.1-fold increase in the carrier density, together with the promoted charge transfer of O_d-VO compared to *p*-VO, are revealed by the negative slope of the Mott-Schottky plots (Figure S21) and electrochemical impedance spectroscopy (EIS; Figure S20b).

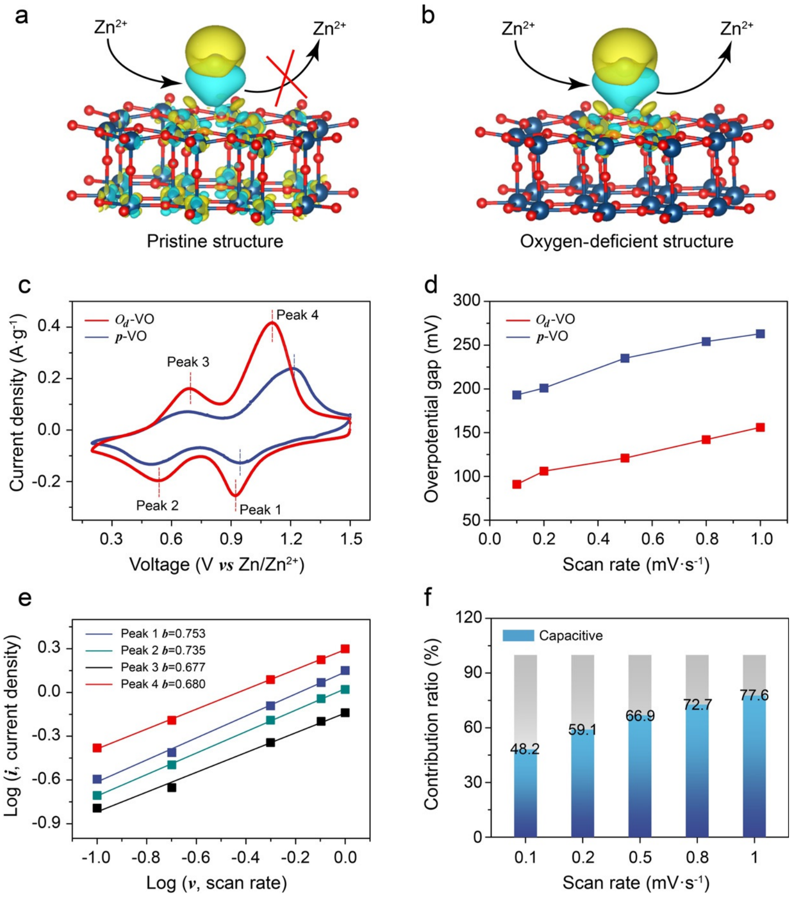

Figure 4. a,b) Illustrations of the Zn^{2+} storage/release for perfect vanadium oxide (*p*-VO) and O_d-VO, respectively. c) Typical CV curves at 0.2 mV s^{-1} of O_d-VO and *p*-VO electrodes after charge/discharge cycling. d) Overpotential gaps of the first redox pair (that is, peaks 1 and 4 labeled in (c) at 0.2 mV s^{-1}). e) Plots of log(i) versus log(v) of the cathodic current response at four peaks of O_d-VO labeled in (c). The slopes of the fitted lines determine the b values. f) Percentages of capacitive contributions of O_d-VO at increasing scan rates.

The introduction of anion/cation vacancies is effective in providing additional pathways for facilitated mobility of Li^+/Na^+ ion in aqueous electrolytes.[32–34] Surface electron density difference analysis was used to understand the modulation of O_d-VO in Zn^{2+} storage/release mechanisms. Perfect V_6O_{13} (*p*-VO) exhibited a uniform charge distribution

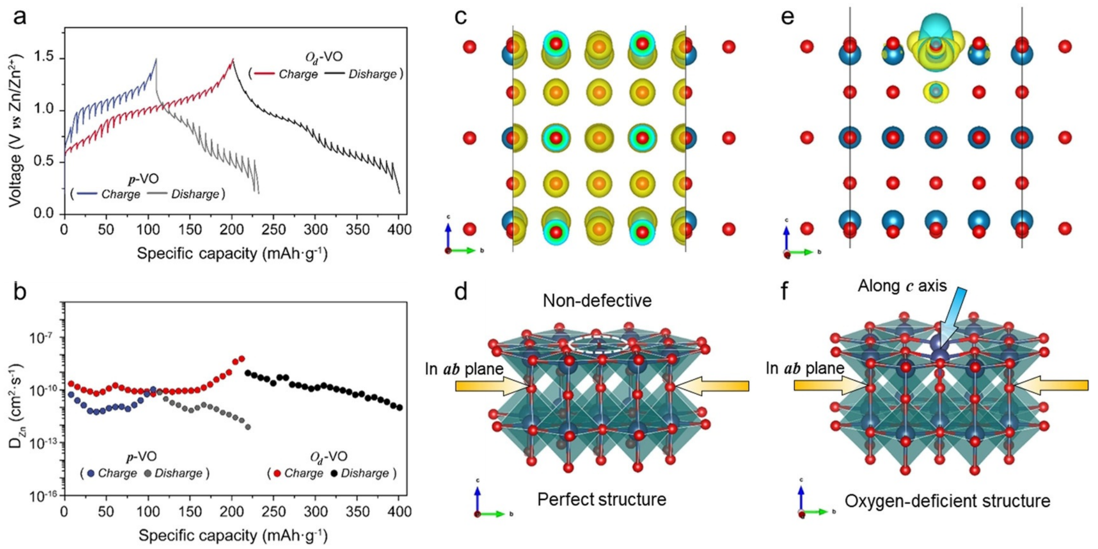

Figure 5. a,b) GITT profiles and calculated Zn^{2+} diffusion coefficient of *p*-VO and O_d-VO electrodes, respectively. c,d) The charge distribution and corresponding structure of *p*-VO. e,f) The charge distribution and corresponding structure of O_d-VO.

(Figures 5 c,d), while electrons accumulated around O_d-VO (Figures 5 e,f). These observations indicate that when the oxygen atoms are extracted from the vanadium oxide lattice, defective sites form with spare electrons, which can then be contributed to the delocalized electron cloud of O_d-VO, leading to an increased capacity.[26] XPS analysis was used to further probe the electrochemical reaction in O_d-VO (Figure S22). In the pristine state, no detectable signal was observed from Zn (Figure S23). Upon discharge, the O_d-VO electrode displayed two Zn $2p_{3/2}$ components located at 1023.4 and 1021.9 eV.[12] The difference of the two Zn sites in binding energies is attributed to the varying interactions with the oxygen atoms in O_d-VO. Based on the greatly enhanced D_{Zn} and capacity of O_d-VO discussed in the preceding text, an oxygen-deficient structure may enable a dual-direction Zn^{2+} insertion. In contrast with regular Zn^{2+} insertion into the *ab* plane of vanadium oxides (yellow arrows in Figures 5 d,f), the oxygen-deficient sites in O_d-VO may open up the vanadium oxide layers to allow Zn^{2+} diffusion/insertion along the *c* axis (blue arrow in Figure 5 f), hence greatly boosting the reaction kinetics and electrochemical reactivity.

In view of the impressive Zn^{2+} storage capability and its binder-free nature, the practicability of O_d-VO was exemplified by fabricating a flexible, quasi-solid-state zinc battery (Figure 6 a). The freestanding O_d-VO and Zn electrode electrodeposited on CC were respectively used as a cathode and an anode with gel electrolyte. The three-dimensional light-weight Zn/CC anode was synthesized to replace conventional Zn foil and thereby suppress formation of dendrites and improve utilization of Zn (Figures S24 and S25). As a consequence of its high flexibility and stability, the bended cell operates well upon deformation (Figure 6 b). Figure 6 c presents the discharge/charge-curve–time characteristics of the pouch-type Zn/O_d-VO battery at 200 mA g^{-1}; it delivered a stable discharge capacity of approximately 195 mAh g^{-1} (based on the O_d-VO cathode and 200 % Zn) with a high capacity retention of 94 % over 50 cycles under varying states of deformation (Figure 6 d), suggesting promising applications in the field of flexible energy storage.

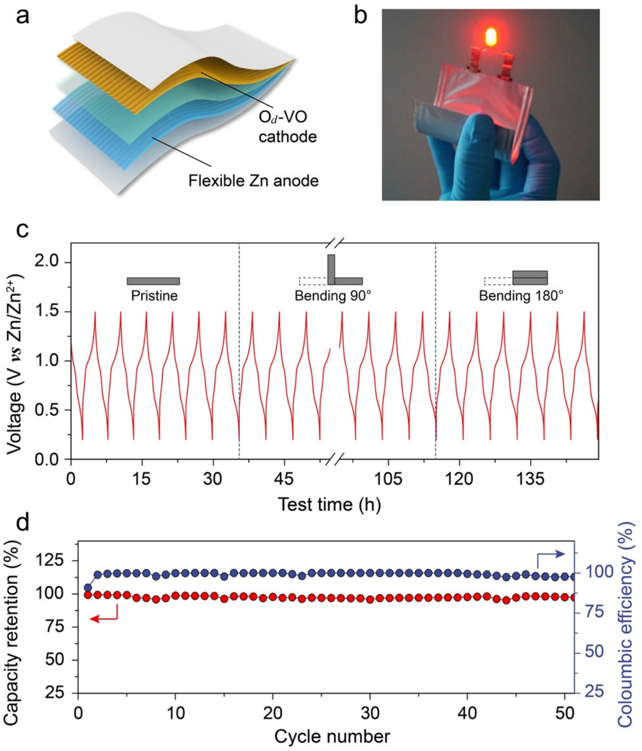

Figure 6. a) A diagram of the flexible Zn/O_d-VO battery chemistry using a O_d-VO cathode and flexible Zn anode. b) Photograph of a flexible soft-package battery powering a light-emitting diode (LED). c) Electrochemical performance of the flexible pouch-type Zn/O_d-VO battery at 200 mA g^{-1} in an unbent state and upon bending by 90° and 180°. d) The corresponding capacity retention and CEs of the flexible Zn/O_d-VO battery in (c).

In summary, a versatile cathode material for high-capacity and long-life AZIBs with high cathode utilization was prepared from oxygen-deficient vanadium oxides. With improved Zn^{2+} reaction kinetics, the resulting cathode shows both high rate capability and desirable cycling performance even at high charge/discharge depth that outperform previously reported cathode materials. It was demonstrated that introduction of oxygen vacancies into the vanadium oxide lattice can efficiently eliminate strong interactions between Zn^{2+} and the host material, thus affording stable cycling performance with high capacity utilization. As a consequence of the flexibility of O_d-VO, a flexible quasi-solid-state Zn/O_d-VO battery was achieved with equally advantageous electrochemical behavior under various bending states. These encouraging performances may open up new methods for advanced cathode design for high-performance AZIBs.

Acknowledgements

This work was supported by MOST (2016YFA0203302), NSFC (21634003, 51573027, 51673043, and 21604012), STCSM (16JC1400702, 17QA1400400, and 18QA1400700), and SHMEC (2017-01-07-00-07-E00062).

Conflict of interest

The authors declare no conflict of interest.

Keywords: aqueous batteries · flexible electronics · oxygen vacancies · rechargeable batteries · vanadium oxide

How to cite: *Angew. Chem. Int. Ed.* **2020**, *59*, 2273–2278
Angew. Chem. **2020**, *132*, 2293–2298

[1] J. Luo, W. Cui, P. He, Y. Xia, *Nat. Chem.* **2010**, *2*, 760–765.
[2] H. Kim, J. Hong, K. Park, H. Kim, S. Kim, K. Kang, *Chem. Rev.* **2014**, *114*, 11788–11827.
[3] F. Wang, O. Borodin, T. Gao, X. Fan, W. Sun, F. Han, A. Faraone, J. A. Dura, K. Xu, C. Wang, *Nat. Mater.* **2018**, *17*, 543–549.
[4] M. Song, H. Tan, D. Chao, H. Fan, *Adv. Funct. Mater.* **2018**, *28*, 1802564.
[5] C. Xu, B. Li, H. Du, F. Kang, *Angew. Chem. Int. Ed.* **2012**, *51*, 933–935; *Angew. Chem.* **2012**, *124*, 957–959.
[6] H. Pan, Y. Shao, P. Yan, Y. Cheng, K. Han, Z. Nie, C. Wang, J. Yang, X. Li, P. Bhattacharya, K. T. Mueller, J. Liu, *Nat. Energy* **2016**, *1*, 16039.
[7] J. Huang, W. Zhuo, M. Hou, X. Dong, L. Yao, Y. Wang, Y. Xia, *Nat. Commun.* **2018**, *9*, 2906.
[8] T. Xiong, Z. Yu, H. Wu, Y. Du, Q. Xie, J. Chen, Y. Zhang, S. J. Pennycook, W. Lee, J. Xue, *Adv. Energy Mater.* **2019**, *9*, 1803815.
[9] H. Li, Z. Liu, G. Liang, Y. Huang, Y. Huang, M. Zhu, Z. Pei, Q. Xue, Z. Tang, Y. Wang, B. Li, C. Zhi, *ACS Nano* **2018**, *12*, 3140–3148.
[10] G. Fang, C. Zhu, M. Chen, J. Zhou, B. Tang, X. Cao, X. Zheng, A. Pan, S. Liang, *Adv. Funct. Mater.* **2019**, *29*, 1808375.
[11] H. Zhang, J. Wang, Q. Liu, W. He, Z. Lai, X. Zhang, M. Yu, Y. Tong, X. Lu, *Energy Storage Mater.* **2019**, *21*, 154–161.
[12] M. Yan, P. He, Y. Chen, S. Wang, Q. Wei, K. Zhao, X. Xu, Q. An, Y. Shuang, Y. Shao, K. T. Mueller, L. Mai, *Adv. Mater.* **2018**, *30*, 1703725.
[13] N. Zhang, Y. Dong, M. Jia, X. Bian, Y. Wang, M. Qiu, J. Xu, Y. Liu, L. Jiao, F. Cheng, *ACS Energy Lett.* **2018**, *3*, 1366–1372.
[14] D. Kundu, B. D. Adams, V. Duffort, S. H. Vajargah, L. F. Nazar, *Nat. Energy* **2016**, *1*, 16119.
[15] N. Zhang, M. Jia, Y. Dong, Y. Wang, J. Xu, Y. Liu, L. Jiao, F. Cheng, *Adv. Funct. Mater.* **2019**, *29*, 1807331.
[16] F. Wan, L. Zhang, X. Dai, X. Wang, Z. Niu, J. Chen, *Nat. Commun.* **2018**, *9*, 1656.
[17] C. Xia, J. Guo, Y. Lei, H. Liang, C. Zhao, H. N. Alshareef, *Adv. Mater.* **2018**, *30*, 1705580.
[18] H. Pan, G. Zhang, X. Liao, M. Yan, L. Mai, *Adv. Energy Mater.* **2018**, *8*, 1702463.
[19] J. Park, J. Jo, Y. Aniskevich, A. Bakavets, G. Ragoisha, E. Streltsov, J. Kim, S. Myung, *Chem. Mater.* **2018**, *30*, 6777–6787.
[20] X. Dai, F. Wan, L. Zhang, H. Cao, Z. Niu, *Energy Storage Mater.* **2019**, *17*, 143–150.
[21] L. Zhang, L. Chen, X. Zhou, Z. Liu, *Adv. Energy Mater.* **2015**, *5*, 1400930.
[22] Q. Zhao, W. Huang, Z. Luo, L. Liu, Y. Lu, Y. Li, L. Li, J. Hu, H. Ma, J. Chen, *Sci. Adv.* **2018**, *4*, eaao1761.
[23] W. Li, K. Wang, S. Cheng, K. Jiang, *Energy Storage Mater.* **2018**, *15*, 14–21.
[24] F. Wan, Z. Niu, *Angew. Chem. Int. Ed.* **2019**, *58*, 16358–16367; *Angew. Chem.* **2019**, *131*, 16508–16517.
[25] P. Liu, K. Zhu, Y. Gao, H. Luo, L. Lu, *Adv. Energy Mater.* **2017**, *7*, 1700547.
[26] G. Fang, J. Zhou, A. Pan, S. Liang, *ACS Energy Lett.* **2018**, *3*, 2480–2501.
[27] B. Jiang, Y. He, B. Li, S. Zhao, S. Wang, Y. He, Z. Lin, *Angew. Chem. Int. Ed.* **2017**, *56*, 1869–1872; *Angew. Chem.* **2017**, *129*, 1895–1898.
[28] S. Zhao, Z. Wang, Y. He, B. Jiang, Y. Harn, X. Liu, F. Yu, F. Feng, Q. Shen, Z. Lin, *ACS Energy Lett.* **2017**, *2*, 111–116.
[29] S. Zhao, Z. Wang, Y. He, H. Jiang, Y. Harn, X. Liu, C. Su, H. Jin, S. Wang, Q. Shen, Z. Lin, *Adv. Energy Mater.* **2019**, *9*, 1901093.
[30] Y. Ding, Y. Wen, C. Wu, P. Aken, J. Maier, Y. Yu, *Nano Lett.* **2015**, *15*, 1388–1394.
[31] Y. Song, T. Liu, B. Yao, T. Kou, D. Feng, X. Liu, Y. Li, *Small* **2017**, *13*, 1700067.
[32] C. Li, G. Melaet, W. Ralston, K. An, C. Brooks, Y. Ye, Y. Liu, J. Zhu, J. Guo, S. Alayoglu, G. A. Somorjai, *Nat. Commun.* **2015**, *6*, 6538.
[33] Y. Zou, W. Zhang, N. Chen, S. Chen, W. Xu, R. Cai, C. L. Brown, D. Yang, X. Yao, *ACS Nano* **2019**, *13*, 2062–2071.
[34] T. Koketsu, J. Ma, B. J. Morgan, M. Body, C. Legein, W. Dachraoui, M. Giannini, A. Demortière, M. Salanne, F. Dardoize, H. Groult, O. Borkiewicz, K. Chapman, P. Strasser, D. Dambournet, *Nat. Mater.* **2017**, *16*, 1142–1148.

Manuscript received: September 24, 2019
Revised manuscript received: November 2, 2019
Accepted manuscript online: November 19, 2019
Version of record online: December 27, 2019